Integration of Coherence and Volumetric Curvature Images

Satinder Chopra*

Arcis Corporation, Calgary, Canada

schopra@arcis.com

and

Kurt J. Marfurt

The University of Oklahoma, Norman, US

Summary

Volumetric attributes computed from 3D seismic data are powerful tools in the prediction of fractures and other stratigraphic features. Geologic structures often exhibit curvature of different wavelengths. Curvature images having different wavelengths provide different perspectives of the same geology. Tight (short-wavelength) curvature often delineates details within intense, highly localized fracture systems. Broad (long wavelength) curvature often enhances subtle flexures on the scale of 100-200 traces that are difficult to see in conventional seismic, but are often correlated to fracture zones that are below seismic resolution, as well as to collapse features and diagenetic alterations that result in broader bowls. Such multi-spectral volumetric estimates of curvature are very useful for seismic interpreters and we depict a number of example demonstrating such applications.

Introduction

Computation of volumetric curvature attributes is a significant advancement in the field of attributes. Initial curvature applications were limited to picked 3D seismic horizons. In addition to delineating faults (Sigismundi and Soldo) and subtle carbonate buildups (Hart, 2003), horizon-based curvature has been correlated to open fractures measured on outcrops (Lisle, 1994) and to production data (Hart et al., 2002). Horizon-based curvature is limited not only by the interpreter's ability to pick, but also the existence of horizons of interest at the appropriate level in 3D seismic data volumes. Horizon picking can be a challenging task in datasets contaminated with noise and where rock interfaces do not exhibit a consistent impedance contrast amenable to human interpretation. To address this issue, Al-Dossary and Marfurt (2006) generated volumetric estimates of curvature generated from volumetric estimates of reflector dip and azimuth. Such reflector dip and azimuth estimates can be calculated using a complex trace analysis (Barnes, 2000), a gradient-structure tensor, discrete semblance-based searches (Marfurt 2006), or plane-wave destructor techniques (Fomel, 2008). Computing derivatives of the volumetric reflector dip components provides a full 3D volume of curvature values. There are many curvature measures that can be computed, with several authors finding a good correlation between dip curvature (in the Austin chalk), strike curvature (Hart et al., 2002), and Gaussian curvature (Lisle, 1994) to open fractures. However, in general curvature is

an excellent measure of paleo deformation. With an appropriate tectonic deformation model, a good structural geologist can predict where fractures were formed. However, since their formation, such fractures may have been cemented (Rich, 2008), filled with overlying sediments (Nissen, 2006) or diagenetically altered (Nissen et al., 2007). Furthermore, the present-day direction of minimum horizontal stress may have rotated from the direction at the time of deformation, such that previously open fractures are now closed, while previously closed fractures may now be open. For this reason, prediction of open fractures requires not only images of faults and flexures provided by coherence and curvature coupled with an appropriate model of deformation, but also measures of present day stress provided by breakouts seen in image lots and seismic anisotropy measures.

Many workers will prefer using maximum and minimum curvature (e.g. Sigismundi and Soldo, 2003; Klein et al., 2008), while others (including the authors) have preferred using the most-positive and most-negative curvatures. In this paper, we propose simply using the principal curvatures, k_1 and k_2, which we describe below. In addition to faults and fractures, stratigraphic features such as levees and bars and diagenetic features such as karst collapse and hydrothermally altered dolomites also appear to be well-defined on curvature displays. Channels appear when differential compaction has taken place.

A review of curvature definitions

Sigismondi and Soldo (2003) provide an easy-to-understand definition of curvature of a 2D surface:

$$k_{2D} = \frac{1}{R} = \frac{\frac{d^2z}{dx^2}}{\left[1+\left(\frac{dz}{dx}\right)^2\right]^{3/2}}, \qquad (1)$$

where R is the radius of curvature and $z(x)$ is the elevation of a 2D horizon. 2D curvature is defined as the change in the radius of curvature, and hence of the angle of the normal with the vertical, $\varphi = \tan^{-1}(z/x)$. We raise two pitfalls for those wishing to correlate equation 1 to curvature definitions found in 3D solid geometry references. First, geoscientists, petroleum engineers and mining engineers are unique in that they point the positive z or t axis *down*, rather than *up*, like the rest of the world. Thus anticlinal features will have a positive value of 2D curvature and synclinal features will have a negative value of 2D curvature. Second, most of us learned in calculus that the curvature of a function z(x) is simply

$$c_{2D} = \frac{d^2z}{dx^2}. \qquad (2)$$

Sigismondi and Sold (2003) show that the peak values of equation 2 will occur at the crest of a folded 2D image, while the peak values of equation 1 will occur at the position of tightest curvature having a positive value.

In 3D, we encounter somewhat more difficult to visualize formulae. We use Roberts (2001) notation and assume we fit a picked horizon with a quadratic surface of the form:

$z(x,y)=ax^2+cxy+by^2+dx+ey+f$. (3)

Roberts (2001) then goes on to define the mean curvature, k_{mean}, Gaussian curvature, k_{Gauss}, and principal curvatures, k_1 and k_2:

$k_{mean}=[a(1+-e^2)+b(1+-d^2)-cde]/(1+d^2+e^2)^{3/2}$, (4)

$$k_{Gauss}=(4ab-c^2)/(1+d^2+e^2)^2, \qquad (5)$$

$$k_1 = k_{mean} + (k_{mean}^2 - k_{Gauss})^{1/2}, \qquad (6)$$

$$k_2 = k_{mean} - (k_{mean}^2 - k_{Gauss})^{1/2}, \qquad (7)$$

Note that k_1 is a *signed value* that is always greater than or equal to k_2. However, most references on solid geometry define the maximum curvature as the first eigenvalue of a Hessian matrix equation defining the quadratic surface (e.g. Rich, 2008). Recall that in principal component analysis, the eigenvalue defines the *unsigned* magnitude of the deformation, while the eigenvector defines its sign and shape. For this reason, Roberts (2001) uses the classical definition of the maximum and minimum curvatures, k_{max} and k_{min}

$$k_{max} = \begin{cases} k_1 \text{ if } |k_1| \geq |k_2| \\ k_2 \text{ if } |k_1| < |k_2| \end{cases}, \text{ and} \qquad (8)$$

$$k_{min} = \begin{cases} k_2 \text{ if } |k_1| \geq |k_2| \\ k_1 \text{ if } |k_1| < |k_2| \end{cases}. \qquad (9)$$

While these formulae are a 3D generalization of equation 1, it causes considerable confusion for those of us who come from a geology vs. mathematics background. First, the maximum curvature will not always have a positive value. If we have an elongated synclinal bowl, the maximum curvature will actually be the curvature of the shortest cross section, while the minimum curvature will be the curvature in the strike direction of our basin. For this reason, several authors (including many of our publications) have favored using the most-positive, $k_{pos,}$ and most-negative curvature k_{neg}:

$$k_{pos} = (a+b)+[(a-b)^2 + c^2]^{1/2}, \text{ and} \qquad (10)$$

$$k_{neg} = (a+b)-[(a-b)^2 + c^2]^{1/2}. \qquad (11)$$

Equations 6 and 7 correspond to equation 1 and equations 10 and 11 correspond to equation 2. For relatively flat dips, such as encountered in the Fort Worth Basin and Permian Basins of Texas (Al-Dossary and Marfurt, 2006; Blumentritt et al., 2006) $k_{pos} \approx k_1$ and $k_{neg} \approx k_2$. However, in highly deformed areas such as the deeper Chicontepec Basin of Mexico (Mai et al., 2009) the differences can be significant. By using the principal curvatures k_1 and k_2, we maintain the accuracy for highly deformed terraines of k_{max} and k_{min}, while providing the interpretational simplicity of k_{pos} and k_{min}. We also hope to eliminate the confusion on the definition of k_{max} and k_{min}, with several commercial software vendors implementing them not as defined by Roberts (2001) and the mathematical literature, but rather as we have defined k_1 and k_2.

Multi-spectral volumetric estimation of curvature

Multispectral curvature estimates introduced by Bergbauer et al. (2003) and extended to volumetric calculations by Al Dossary and Marfurt (2006) can yield both long and short wavelength curvature images, allowing an interpreter to enhance geologic features having different scales. Tight (short-wavelength) curvature often delineates details within intense, highly localized fracture systems. Broad (long wavelength) curvature often enhances subtle flexures on the scale of 100-200 traces that are difficult to see in conventional seismic, but are often correlated to fracture zones that are below seismic resolution, as well as to collapse features and diagenetic alterations that result in broader bowls. We describe some applications of multi-spectral volumetric estimates of curvature in Chopra and Marfurt (2007).

Examples

Appearance of folds and faults

Figure 1 shows corresponding horizon slices through the maximum curvature, k_{max}, and the principal curvature k_1, defined by equations 6 and 7. Note that the principal curvature is much more continuous than the maximum curvature. For this reason, many authors favor these displays when mapping stratigraphic features (e.g. Chopra and Marfurt, 2008) as well as subtle faults and fractures in the presence of gentle dip (e.g. Sullivan et al., 2006; Nissen et al., 2007). However, in areas of folding in the presence of significant dip, the crest and trough of a fold defined as the highest and lowest points on a vertical section no longer correspond to the locations of the tightest folding. For this reason, we propose using the principal curvatures, k_1 and k_2.

Appearance of fractures

In Figure 2 we show an inline and a crossline from a 3D seismic volume from Alberta. This data volume was used for the study of fractures at the level indicated with the blue vertical arrow. The fractures in the indicated formation manifest on the seismic in the form of broken down reflections. Consequently, the coherence display (Figure 3a) shows low coherence in this zone on the time slice. The long-wavelength most-positive curvature (Figure 3b) indicates the main reflection trends in the form of red lineaments. This pattern is interspersed with blue broken trends which are seen very clearly on the long-wavelength most-negative curvature display in Figure 3c. The short-wavelength version of the two curvature displays as seen in Figures 3c and e show these lineaments in a lot more detail as would be expected for fractured zones.

It is always a good idea to calibrate the interpretation on curvature displays with log data if possible. One promising way is to interpret the lineaments in a fractured zone and then transform them into a rose diagram. Such rose diagrams can then be compared with similar rose diagrams that are obtained from image well logs to gain confidence in the seismic-to-well calibration. Once a favorable match is obtained, the interpretation of fault/fracture orientations and the thicknesses over which they extend can be used with greater confidence for more quantitative reservoir analysis. Needless to mention such calibrations need to be carried out in localized areas around the wells for accurate comparisons.

Figure 4 shows how the generation of rose diagrams from the long-wavelength and the short-wavelength displays. Notice the rose diagram generated from the short-wavelength curvature display leads to a more robust display, than the sparse lineament seen on the long-wavelength display.

Appearance of incised channels

In Figure 5 we show a comparison of coherence with the long-wavelength and short-wavelength versions of the k_1 and k_2 curvature. Notice a meandering channel seen on the coherence display (Figure 5a), which has its levees seen clearly at some points but not so well defined at others (yellow arrows). In Figure 5b showing the long-wavelength version of the k_1 curvature, we see some of the levees of the channel developed as indicated by the yellow arrows. The axis or the thalweg of the channel is seen very clearly on the long-wavelength version of the k_2 curvature in Figure 5c. As expected, enhanced resolution in terms of

definition of the channel is seen on the short-wavelength version of both the k_1 and k_2 curvature as seen in Figure 5d and e.

Differential compaction

Not all channels result in negative curvature anomalies. The feature shown in Figure 6 clearly appears to be a channel on the coherence image, but appears as a positive curvature anomaly along the channel axis. Such an anomaly is due to differential compaction. In this case, the channel axis is filled with sand and the matrix with shale. Over geologic time, the shale has compacted more than the sand-filled channel, resulting in a local high. Such anomalies are common in the North Sea and other parts of the world where sufficient time has passed to produce differential compaction.

Conclusions

Volumetric curvature is a well-established interpretational tool that allows us to image subtle faults, folds, incised channels, differential compaction, and a wide range of other stratigraphic features. The maximum and minimum curvatures define the eigenvalues of a quadratic surface. By definition (and based on eigenstructure analysis), the maximum curvature is defined as the principal curvature that has the larger absolute. However, we find that the principal curvatures k_1 and k_2, where $k_1 \geq k_2$, provide the simplicity of interpretation seen in k_{pos} and k_{neg}, but retain the robustness of k_{max} and k_{min} in the presence of steep dip.

Multispectral volumetric curvature attributes are valuable for prediction of fracture lineaments in deformed strata. Several applications of volume curvature have been completed in different geological settings, which are found to be useful for different stratigraphic features, ranging from imaging of channel boundaries, small scale faults to highly fractured zones.

Acknowledgements

References

Al-Dossary, S., and K. J. Marfurt, 2005, 3-D volumetric multispectral estimates of reflector curvature and rotation: Geophysics, **71**, P41-P51.

Barnes, A. E., 2000a, Weighted average seismic attributes: Geophysics, **65**, 275–285.

Bergbauer, S., T. Mukerji, and P. Hennings, 2003, Improving curvature analyses of deformed horizons using scale-dependent filtering techniques: AAPG Bulletin, **87**, 1255-1272.

Chopra, S., and K. J. Marfurt, 2007, Volumetric curvature attributes for fault/fracture characterization: First Break, **25**, 35-46.

Chopra, S., and K. J. Marfurt, 2008, Emerging and future trends in seismic attributes: The Leading Edge, **27**, 298-318.

Blumentritt, C., K. J. Marfurt, and E. C. Sullivan, 2006, Volume-based curvature computations illuminate fracture orientations, Lower-Mid Paleozoic, Central Basin Platform, West Texas: Geophysics, **71**, B159-B166.

Fomel, S., 2008, Predictive painting of 3D seismic volumes: 77th Annual International Meeting of the SEG, Expanded Abstracts, 864-868.

Hart, B.S., R. Pearson, R. Pearson, and G. C. Rawling, 2002, 3-D seismic horizon-based approaches to fracture-swarm sweet spot definition in tight-gas reservoirs: The Leading Edge, **21,** 28-35.

Klein, P., L. Richard, and H. James, 2008, 3D curvature attributes: a new approach for seismic interpretation: First Break, 26, 105-111.

Lisle, R. J., 1994, Detection of zones of abnormal strains in structures using Gaussian curvature analysis: AAPG Bulletin, 78, 1811-1819.

Marfurt, K. J., 2006: Robust estimates of reflector dip and azimuth: Geophysics, 71, P29-P40.

Mai, H., K. J. Marfurt, and S. Chávez-Pérez , 2009 Coherence and volumetric curvatures and their spatial relationship to faults and folds, an example from Chicontepec basin, Mexico: 78th Annual International Meeting of the SEG, Expanded Abstracts,xx-yy.

Nissen, S. E., Carr, T. R., Marfurt, K. J., and Sullivan, E. C,, 2007, Using 3-D seismic volumetric curvature attributes to identify fracture trends in a depleted Mississippian carbonate reservoir: Implications for assessing candidates for CO_2 sequestration, in M. Grobe, J. Pashin, and R. Dodge, eds., Carbon Dioxide Sequestration in Geological Media--State of the Art: Special Publication, American Assoc. of Petroleum Geologists.

Rich, J., 2008, Expanding the applicability of curvature attributes through clarification of ambiguities in derivation and terminology: 77th Annual International Meeting of the SEG, 884-887.

Roberts, A., 2001, Curvature attributes and their application to 3D interpreted horizons. First Break, **19**, 85-99.

Sigismondi, E.M., and C. J. Soldo, 2003, Curvature attributes and seismic interpretation: Case studies from Argentina basins: The Leading Edge, 22, 1122-1126.

Sullivan, E. C., K. J. Marfurt, A. Lacazette, and M. Ammerman, 2006, Application of New Seismic Attributes to Collapse Chimneys in the Fort Worth Basin: Geophysics, **71**, B111-B119.
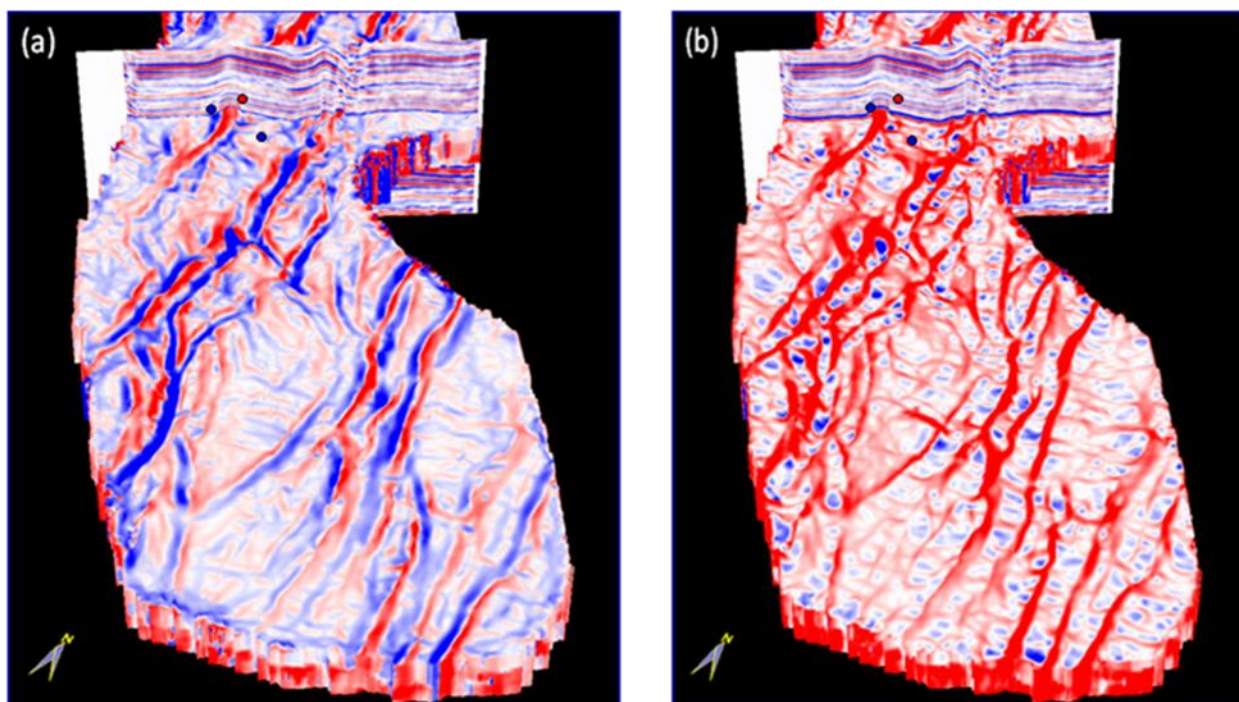
1: Vertical section through a faulted volume. Blue circles indicate the synclinal features while red circle indicates anticlinal feature defining a downthrown graben. Horizon slices through volumes of (a) maximum curvature, k_{max}, and (b) most-positive curvature. Many workers like using maximum curvature since they can easily visualize anomalies that correspond to up-thrown and down-thrown faulting, straddling the fault discontinuity.
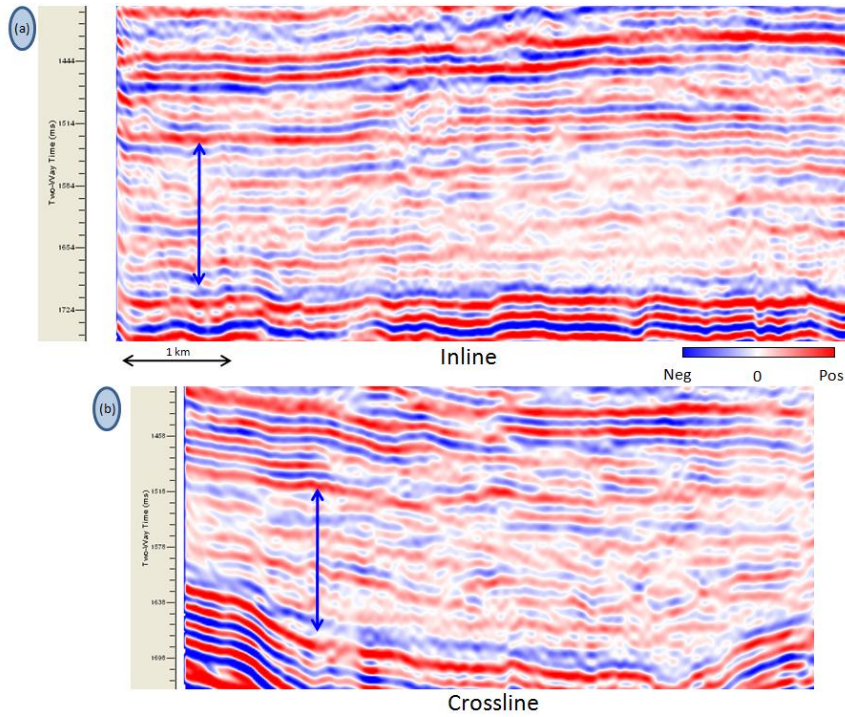
Figure 2: An inline and a crossline from a 3D seismic data volume from Alberta. The vertical blue arrows indicate the fractured zone on the seismic section.
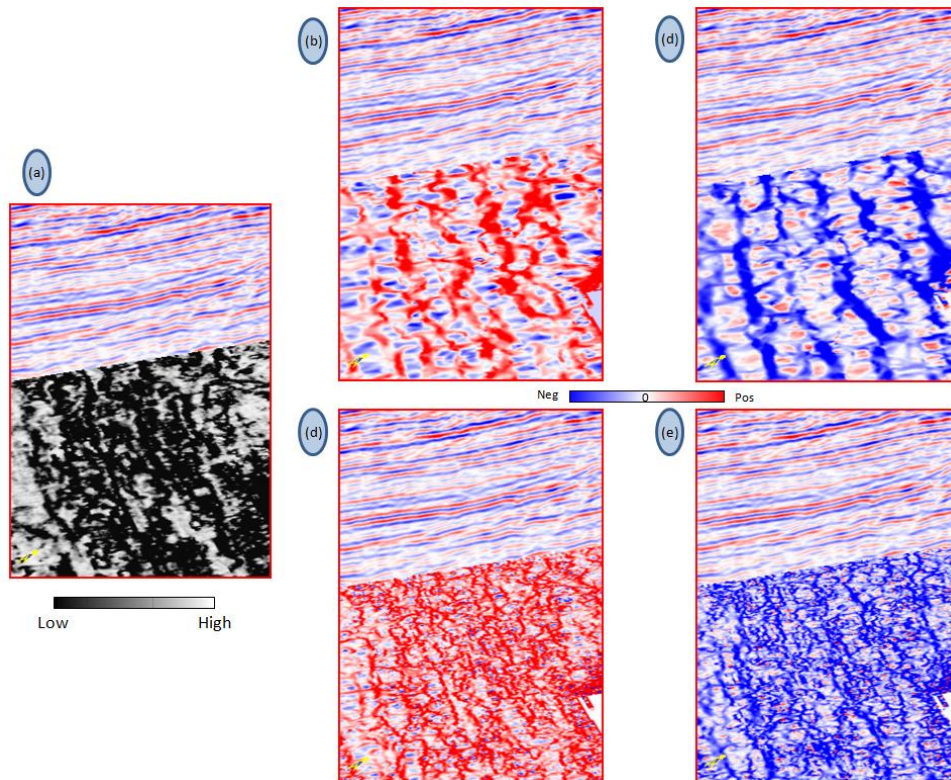

Figure 3: Zoom of chair-displays where the vertical display is a portion of a crossline through the original 3D seismic amplitude volume while the horizontal displays are time slices through (a) coherence (b) most-positive (long-wavelength) (c) most-positive (short-wavelength), (d) most-negative (long-wavelength) and (e) most-negative (short-wavelength) attribute volumes.
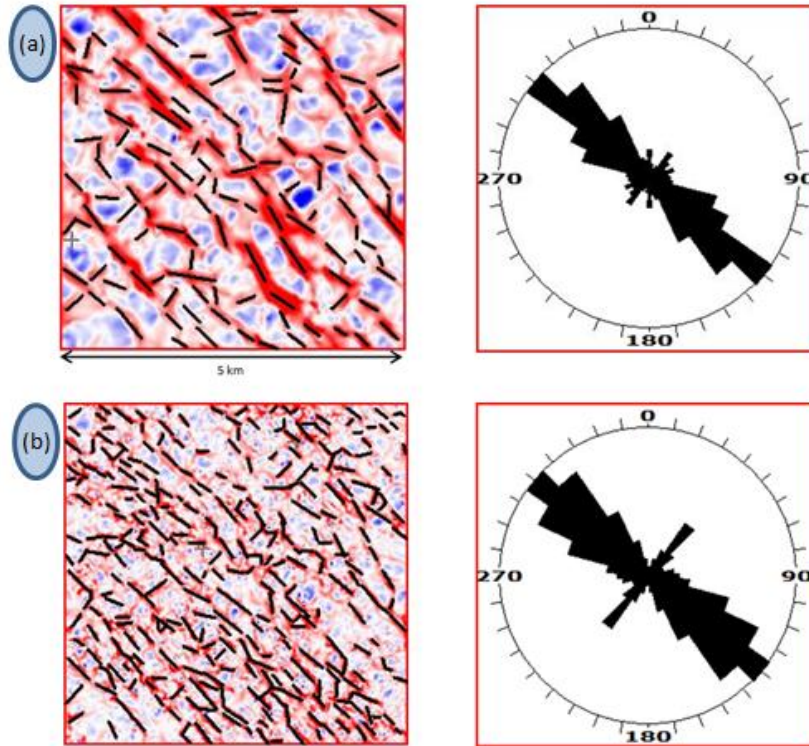
Figure 4: A time slice through the most-positive curvature (a) long-wavelength volume and (b) short-wavelength volume, with the individual lineaments interpreted in black. The rose diagram prepared for these set of lineaments in black are shown to the right of each figure.
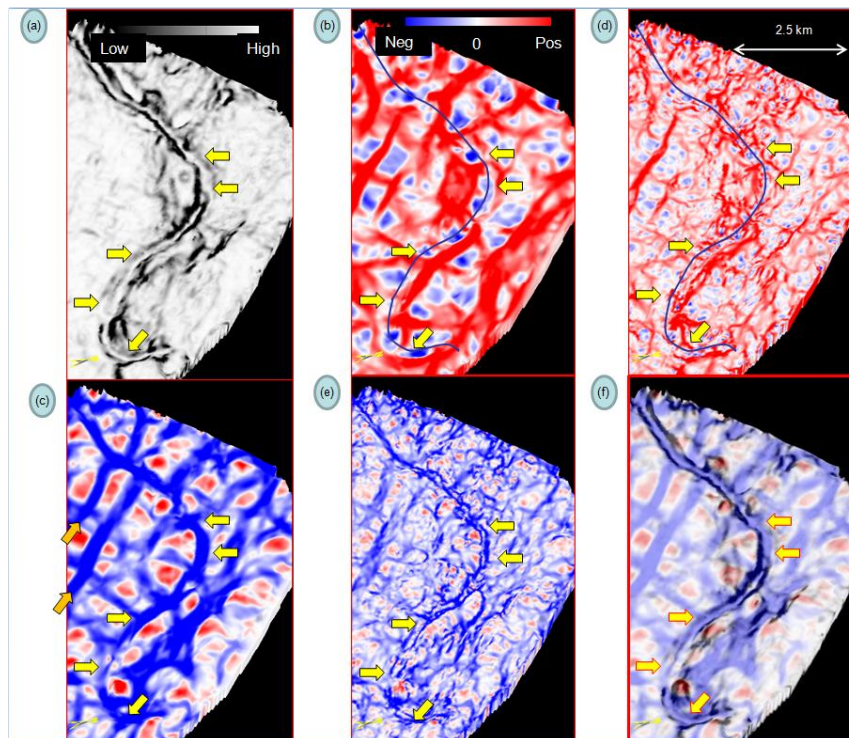

Figure 5: Stratal slices showing an incised channel system through (a) coherence (b) k_1 (c) k_2 (long-wavelength) (d) k_1 (short-wavelength) (e) k_2 (short-wavelength) and (f) co-rendered coherence and k_2 (long-wavelength) volumes. The definition detail on the long-wavelength curvature attribute displays is higher and focused than similar lineaments on the coherence display.
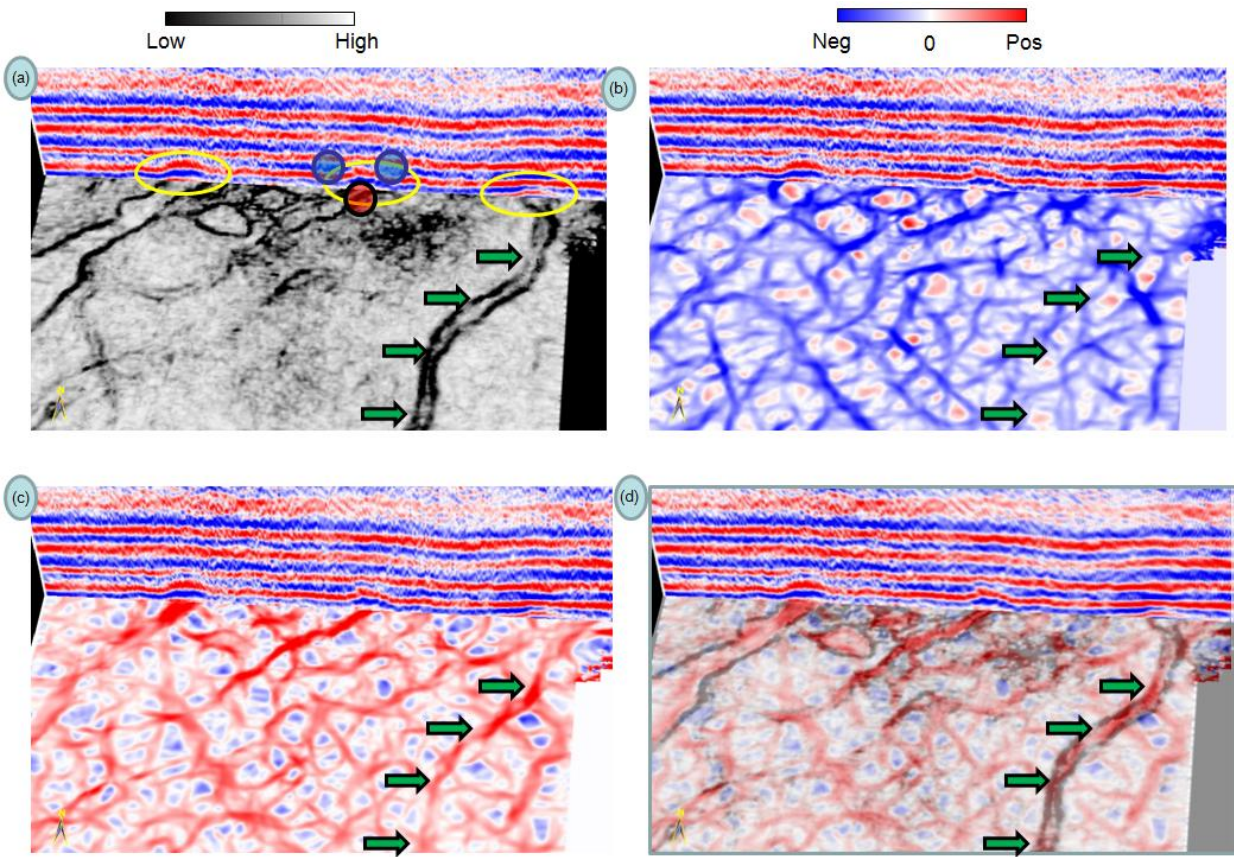
Figure 6: Not all incised valleys result in negative curvature anomalies. In this example from Alberta, Canada, we see positive features associated with the channel axes indicating that the channel is filled with sand and the surrounding matrix with a more easily compactable shale. (a) coherence (b) long-wavelength k_1 (c) long-wavelength k_2 (d) co-rendered coherence and long-wavelength k_1 volumes.